

Article

Performance Improvement of Grid-Connected Induction Motors through an Auxiliary Winding Set

Luigi Danilo Tornello¹, Salvatore Foti² , Mario Cacciato^{1,*}, Antonio Testa², Giacomo Scelba¹ ,
Salvatore De Caro², Giuseppe Scarcella¹ and Santi Agatino Rizzo¹ 

¹ Department of Electrical Electronic and Computer Engineering, University of Catania, 95125 Catania, Italy; luigi.tornello@unict.it (L.D.T.); giacomo.scelba@unict.it (G.S.); giuseppe.scarcella@unict.it (G.S.); santi.rizzo@unict.it (S.A.R.)

² Department of Engineering, University of Messina, 98166 Messina, Italy; sfoti@unime.it (S.F.); atesta@unime.it (A.T.); sdecaro@unime.it (S.D.C.)

* Correspondence: mario.cacciato@unict.it

Abstract: A technique to improve the performance of grid-connected induction motors by exploiting an auxiliary winding set is proposed in this paper. This auxiliary winding features the same distribution of the main winding, although with a reduced number of turns and it is fed by an inverter a fraction of the power in comparison with the rated size of the induction motor. As shown in the paper, through the auxiliary winding, it is possible to set the machine power factor, increasing the efficiency of the power conversion system and mitigating speed oscillations due to torque disturbances. A mitigation of the grid current peaks due to motor start-up is obtainable. First, the proposed technique is theoretically introduced, then a feasibility assessment is accomplished by simulations.

Keywords: power factor correction; efficiency; induction machines; pulse width modulation inverters; dual stator winding machines; harmonic compensation



Citation: Tornello, L.D.; Foti, S.; Cacciato, M.; Testa, A.; Scelba, G.; De Caro, S.; Scarcella, G.; Rizzo, S.A. Performance Improvement of Grid-Connected Induction Motors through an Auxiliary Winding Set. *Energies* **2021**, *14*, 2178. <https://doi.org/10.3390/en14082178>

Academic Editor:
Emilio Gomez-Lazaro

Received: 1 March 2021
Accepted: 6 April 2021
Published: 13 April 2021

Publisher's Note: MDPI stays neutral with regard to jurisdictional claims in published maps and institutional affiliations.



Copyright: © 2021 by the authors. Licensee MDPI, Basel, Switzerland. This article is an open access article distributed under the terms and conditions of the Creative Commons Attribution (CC BY) license (<https://creativecommons.org/licenses/by/4.0/>).

1. Introduction

The replacement of obsolete electric motors with new, more efficient ones could provide considerable advantages in terms of polluting emissions, energy resources exploitation, and manufacturing costs. For this reason, the mandatory compliance of industrial electromechanical systems with gradually increasing efficiency requisites has been enforced all over the world in the last decades. This can be accomplished either by increasing the efficiency of motors, for example, according to European Union (EU) IE2 and IE3 efficiency levels [1], or by replacing direct online electric motors with electric drives.

Despite the wide variety of electric motors available on the market, low- and medium-power three-phase direct online induction motors (DOL-IM) are by far the most dominant in the industrial sector, providing a wide variety of constant speeds and variable load applications where dynamic response requirements are not critical, such as pumps, fans, and compressors. Affordability, durability, easy functioning, and easy maintenance are some of the major factors driving the ever-increasing demand for induction motors. High-efficiency DOL-IMs [1] in industrial applications provide a significant reduction in energy consumption and environmental impact; however, they are still burdened by a low power factor (PF) at partial loads, which can be only mitigated by adding power factor correction capacitors. Moreover, large in-rush current is very commonly generated at start-up, leading to voltage dip, speed loss, torque pulsations, and possible activation of protection devices. A wide diffusion of variable speed drives (VSDs), featuring either torque or speed control, has been experienced in the past thirty years due to the advances in power electronics technology and control strategies, which have allowed an increase in the efficiency and reliability of electric drives [1–4]. Suitable Pulse Width Modulation (PWM) strategies have been developed that are able to cope with adverse effects related to shaft voltages,

bearing currents, motor insulation breakdown, and electromagnetic interference (EMI) issues [5–11]. However, despite clear advantages achieved in terms of efficiency, induction motor drives are much more expensive than DOL-IMs, leading to the development of some intermediate or hybrid solutions. One of these solutions is represented by direct online double-winding IMs (DOL DWIM) [12–14]. They were proposed to overcome some typical drawbacks of conventional induction motors, mainly poor efficiency and power factor, by exploiting a partial power converter, which means an inverter rated at only a fraction of the motor rated power, cutting the cost. According to the DOL-DWIM approach, a special induction machine is used, encompassing two full sets of stator windings: one being directly connected to the grid and a second one being fed by an inverter supplied through a floating capacitor [12–17]. According to the basic DOL-DWIM configuration, the two winding sets feature the same number of turns; thus, the inverter supplying the second set is rated at the grid voltage, although at remarkably lower power. DOL-DWIMs are generally managed by simple control algorithms, mainly developed in order to control the PF under sinusoidal steady state operation [12–17].

An advanced DOL-DWIM configuration is presented in this paper, aimed at achieving new valuable functions in a cost-effective way, such as dynamic, active, and reactive power control; a reduction in in-rush current; and the mitigation of torsional vibrations generated by periodical torque disturbances or distorted grid voltages [18], which lead to acoustic noise and additional mechanical stress.

As shown in Figure 1, the proposed DOL-DWIM configuration features a grid-connected main winding and an auxiliary three-phase winding set featuring a lower number of turns, located in the same stator slots of the main one. The auxiliary winding is supplied by a voltage inverter featuring a floating DC-bus capacitor. As the auxiliary winding has less turns than the main one, the inverter power and voltage ratings are much lower than those of the motor.

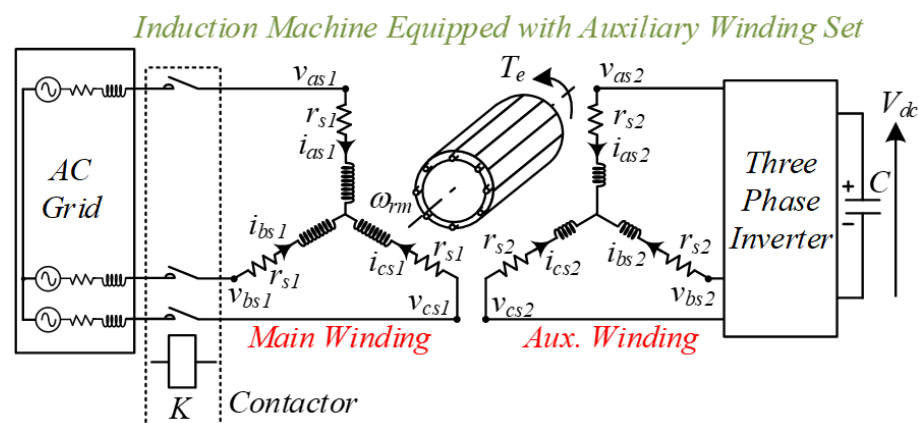


Figure 1. Double-winding induction motor (DWIM) featuring an auxiliary winding set, fed by a three-phase low power, low voltage, Voltage Source Inverter (VSI).

The outline of this paper is as follows: First, the modeling of the electromechanical system is presented in Section 2, and the control strategy implemented in the auxiliary winding set is described in detail in Section 3. Thereafter, the capability of the combined multi-winding sets motor, floating capacitor inverter, and control strategy to efficiently control the power factor PF, mitigate the detrimental effects related to distorted main grid voltages and mechanical torque vibrations, and reduce the large inrush current driven by the induction motor during the starting period is thoroughly investigated in Section 4. Finally, the conclusions are stated in the last section.

2. DWIM Model

It is assumed that the two polyphase stator windings [19–23] are distributed in order to produce sinusoidal magneto-motive forces; moreover, the effects of the saturation of the

magnetic core are neglected, while iron losses are considered according to [24]. The voltage and flux equations of the DOL-DWIM, written in complex form $f_{qd} = f_q - jf_d$, according to an orthogonal qd reference frame rotating at the angular frequency ω_e of the input stator voltage vector, are given by [23]:

$$v_{qds1} = r_{s1}i_{qds1} + \frac{d\lambda_{qds1}}{dt} + j\omega_e\lambda_{qds1} \quad (1)$$

$$v'_{qds2} = r'_{s2}i'_{qds2} + \frac{d\lambda'_{qds2}}{dt} + j\omega_e\lambda'_{qds2} \quad (2)$$

$$v'_{qdr} = r'_r i'_{qdr} + \frac{d\lambda'_{qdr}}{dt} + j(\omega_e - \omega_{re})\lambda'_{qdr} \quad (3)$$

$$\lambda_{qds1} = L_{ls1}i_{qds1} + L_M [i_{qds1} + i'_{qds2} + i'_{qdsr}] \quad (4)$$

$$\lambda'_{qds2} = L'_{ls2}i'_{qds2} + L_M [i_{qds1} + i'_{qds2} + i'_{qdsr}] \quad (5)$$

$$\lambda'_{qdsr} = L'_{lsr}i'_{qdsr} + L_M [i_{qds1} + i'_{qds2} + i'_{qdsr}] \quad (6)$$

$$R_{Fe}i_{qdFe} = \frac{d\lambda'_{qdr}}{dt} + j\omega_e\lambda_{qdm} \lambda_{qdm} = L_M i_{qdm} \quad (7)$$

$$i_{qds1} + i'_{qds2} + i'_{qdsr} = i_{qdm} + i_{qdFe} \quad (8)$$

where v_{qds1} , λ_{qds1} and v'_{qds2} , λ'_{qds2} are the stator voltages and fluxes of the two winding sets, separately; v'_{qdsr} and λ'_{qdr} are the rotor voltages and fluxes, respectively; r'_r , r_{s1} and r'_{s2} are the rotor and stator resistances, respectively; L_M is the mutual inductance; and L'_{lr} , L_{ls1} , and L'_{ls2} are the rotor and stator leakage inductances. All electrical quantities of the auxiliary winding set are referred to in the main stator winding. Moreover, $\omega_{re} = pp\omega_{rm}$, where ω_{rm} is the angular rotor speed and pp is the number of pole pairs. The equivalent circuit of the DWIM is depicted in Figure 2.

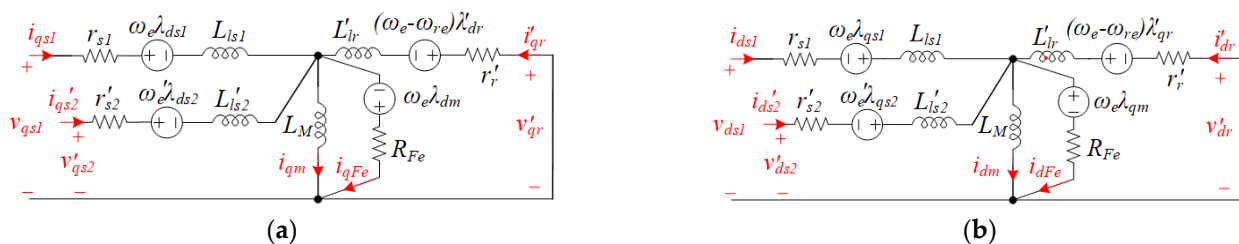


Figure 2. Equivalent circuits of the DWIM in the synchronous reference frame: (a) q-axis and (b) d-axis.

The electromagnetic torque is expressed in Equation (9), [25,26], and the relationships between the total electromagnetic torque T_e applied to the motor shaft and the torque related to the mechanical inertia J , the load torque T_L , and the frictional torque F are described in Equations (10) and (11). θ_{rm} is the rotor position.

$$T_e = 3/2ppL_M[(i_{qs1} + i'_{qs2} - i_{qFe})i'_{dr} - (i_{ds1} + i'_{ds2} - i_{dFe})i'_{qr}] \quad (9)$$

$$T_e = T_L + J \frac{d\omega_{rm}}{dt} + F\omega_{rm} \quad (10)$$

$$\omega_{rm} = \frac{d\theta_{rm}}{dt} \quad (11)$$

3. Control System

The main stator winding set of the DOL DWIM is directly connected to the grid and it is tasked with handling the main power flow toward the mechanical load. Differently, the additional stator winding set is supplied by a floating power inverter, which enables a current vector control according to Figure 3. Low-cost devices are used to measure the AC quantities in both windings. An analysis of the different blocks composing the control system is presented in the following.

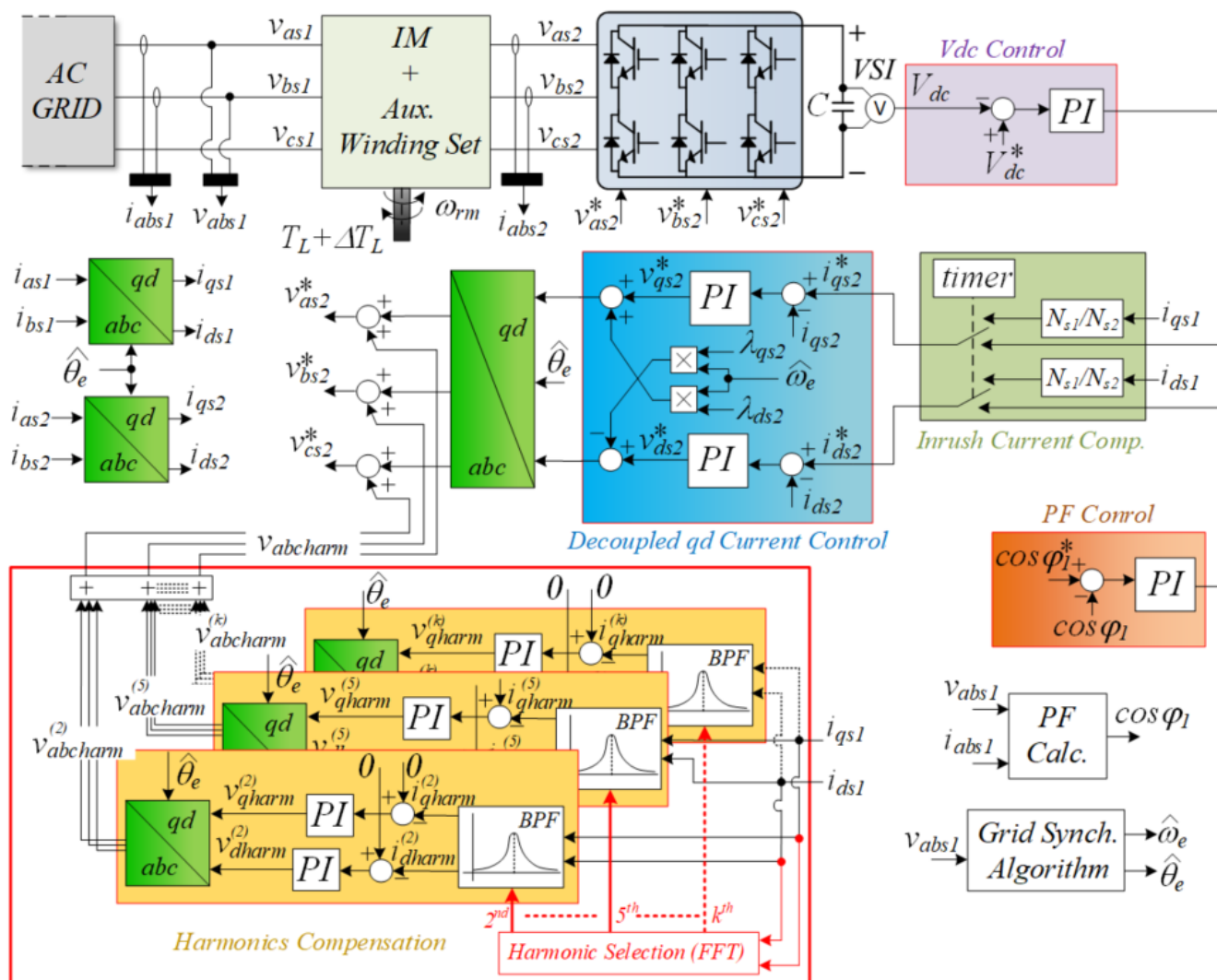


Figure 3. Block diagram of the proposed direct online (DOL) DWIM control solution.

3.1. Grid Synchronization

The control system driving the floating capacitor inverter is mainly based on a standard vector control approach approximating a stator flux orientation, which is achieved by transforming the three-phase utility voltages abc into a reference frame synchronous with the grid voltage vector phase θ_e . The last quantity can be determined with one of the well-known grid synchronization algorithms available in the literature [27,28]. In this work, a decoupling algorithm was exploited to remove all of the unwanted harmonic components from the measured voltages in order to keep the phase-locked loop (PLL) locked to fundamental harmonic, positive-sequence component at all times [29]. The block diagram of the grid synchronization algorithm based on a multi-harmonic synchronous reference frame (SRF) filtering (MSF) structure is shown in Figure 4. The basic idea is to

estimate each voltage harmonic set by applying a low-pass filtering after a reference frame transformation synchronous with the corresponding harmonic frequency.

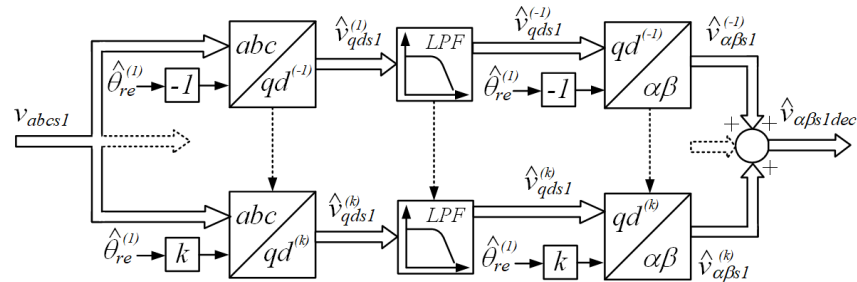


Figure 4. Block diagram of the multiharmonic SRF filtering (MSF) algorithm.

3.2. Active and Reactive Power Control

The machine active and reactive powers are functions of auxiliary winding currents i_{qs2} and i_{ds2} , which can be managed to control the PF under different load conditions. By neglecting the voltage drop due to stator resistances and leakage inductances, the active and reactive power generated by the auxiliary winding can be expressed as:

$$P_2 = 3/2(v_{qs2}i_{qs2} + v_{ds2}i_{ds2}) \quad Q_2 = 3/2(v_{qs2}i_{ds2} - v_{ds2}i_{qs2}) \quad (12)$$

If the $q2$ -axis is aligned to the main grid voltage vector v_{qds1} , the active and reactive power can be approximated to:

$$P_2 = 3/2v_{qs2}i_{qs2} \quad Q_2 = 3/2v_{qs2}i_{ds2} \quad (13)$$

Hence, it is possible to control the machine reactive power by acting on the d-axis current of the auxiliary winding i_{ds2} in order to track a desired power factor at the main stator winding terminals. The q-axis current i_{qs2} can be managed to control the active power required to hold a stable voltage in the floating capacitor of the isolated two-level inverter supplying the auxiliary winding. A certain amount of active power is required by the floating capacitor inverter to compensate for power devices and capacitor losses. Hence, two external control loops were included in the control structure in order to achieve the desired PF and DC bus voltage V_{dc} .

3.3. Active Mitigation of Mechanical Vibrations

The auxiliary winding can be also exploited to mitigate vibrations generated by periodic torque disturbances or distorted grid voltages. Torque disturbances ΔT_L generate harmonic components in the stator currents i_{qs1} and i_{ds1} , yielding vibrations in the mechanical system. They can be mitigated by generating compensating components of the electromagnetic torque by means of the auxiliary winding set. In particular, in case of motor operation under a highly distorted grid voltage, some current harmonics set $i_{as1}^{(k)}$, $i_{bs1}^{(k)}$, $i_{cs1}^{(k)}$ of amplitude I_k and angular frequency $k\omega_e$ are superimposed to the fundamental current set $i_{as1}^l, i_{bs1}^l, i_{cs1}^l$, of magnitude I_1 and angular frequency ω_e . Therefore, it is possible to identify each couple of current harmonic components $i_{qs1}^{(k)}$ and $i_{ds1}^{(k)}$ in the qd current plane by applying a suitable reference frame transformation:

$$\begin{bmatrix} i_{qs1} \\ i_{ds1} \end{bmatrix} = K(\theta_e) \begin{bmatrix} i_{as1} \\ i_{bs1} \\ i_{cs1} \end{bmatrix} = \frac{2}{3} \begin{bmatrix} \cos(\omega_e t) & \cos(\omega_e t - \frac{2}{3}\pi) & \cos(\omega_e t + \frac{2}{3}\pi) \\ \sin(\omega_e t) & \sin(\omega_e t - \frac{2}{3}\pi) & \sin(\omega_e t + \frac{2}{3}\pi) \end{bmatrix} \begin{bmatrix} i_{as1} \\ i_{bs1} \\ i_{cs1} \end{bmatrix} \quad (14)$$

$$\begin{cases} i_{qs1} = i_{qs1}^{(1)} + \sum_{k=1}^{+\infty} i_{qs1}^{(k)} = i_{qs1}^{(1)} + \sum_{k=1}^{+\infty} I_{s1}^{(k)} \cos[(k \pm 1)\omega_e t] \\ i_{ds1} = i_{ds1}^{(1)} + \sum_{k=1}^{+\infty} i_{ds1}^{(k)} = i_{ds1}^{(1)} + \sum_{k=1}^{+\infty} I_{s1}^{(k)} \sin[(k \pm 1)\omega_e t] \end{cases} \begin{cases} +1 \rightarrow \text{if } k = 2, 5, 8, 11, \dots \\ -1 \rightarrow \text{if } k = 4, 7, 10, 13, \dots \\ 0 \rightarrow \text{if } k = 3, 6, 9, 12, \dots \end{cases} \quad (15)$$

where $i_{qs1}^{(1)}$ and $i_{ds1}^{(k)}$ are the DC components related to the fundamental current harmonic. These current harmonics are identified through a standard harmonic identification algorithm based on fast Fourier transform. Each undesired harmonic present on the main winding current is then reproduced with the opposite sign on the auxiliary winding through a specific closed-loop current control. A control structure composed of some parallel current control modules is thus required to mitigate mechanical vibrations featuring different frequencies, each module being threshold-activated on the basis of the actual magnitude of the specific stator current harmonic to be attenuated. Similar considerations are valid in case of mechanical vibrations caused by shaft eccentricity, mechanical imbalance phenomena, or bearing aging.

3.4. Inrush Current Mitigation during Startup

The large line currents that occur on the grid at motor start-up can be mitigated by exploiting the charge stored in the floating capacitor by implementing a proper control strategy in the DOL DWIM. For achieving this additional feature, a suitable selection of the floating capacitor and of the inverter current rating is required. In particular, the inrush current in the main stator winding can be reduced by exploiting the energy stored in the floating capacitor to reduce the power drawn from the grid. This can be accomplished by generating a set of currents exactly in phase with the currents flowing in the main winding during the first few cycles of the grid voltage. The measured main winding currents i_{qs1} and i_{ds1} are firstly scaled by the turn ratio of the two stator windings; then, they are used as references of the closed loop current controllers managing the auxiliary windings voltages in order to generate three phase currents i_{abc2} in phase with i_{abc1} , thus allowing a sharing between the inrush currents of both windings.

4. Performance Assessment of the Grid-Connected DWIM

The control strategies described in the previous section were assessed via a simulation analysis realized in Simulink/MATLAB, as shown in Figure 5a. The model of the electromechanical system, shown in Figure 5b, was realized according to the data listed in Table 1. Implementation of the multiharmonic SRF filter and harmonic compensation system are presented, respectively, in Figure 6a,b. According to Table 1, the considered machine features a turns ratio between the main and auxiliary windings $N_{s1}/N_{s2} = 5$. The floating capacitor inverter was driven with a space vector modulation (SVM) at a switching frequency f_s of 10 kHz and the DC bus voltage control held an average voltage V_{dc} of 150 V. The inverter was equipped with a 5 mF floating DC bus capacitor.

Table 1. Multi-winding induction motor data.

	Winding 1	Winding 2
Stator Voltage V_s	400 Vrms	60 Vrms
Stator Current I_s	25 Arms	60 Arms
Stator Resistance R_s	0.2147 Ω	0.01 Ω
Leakage Inductance L_{ls}	0.991 mH	40 μ H
Rotor Resistance r'_r		0.2205 Ω
Magnetizing Inductance L_M		64.2 mH
Iron Losses Resistance R_{Fe}		700 Ω
Nominal Rotor Speed ω_{rm}		1460 rpm
Mechanical Inertia J		0.102 kgm ²

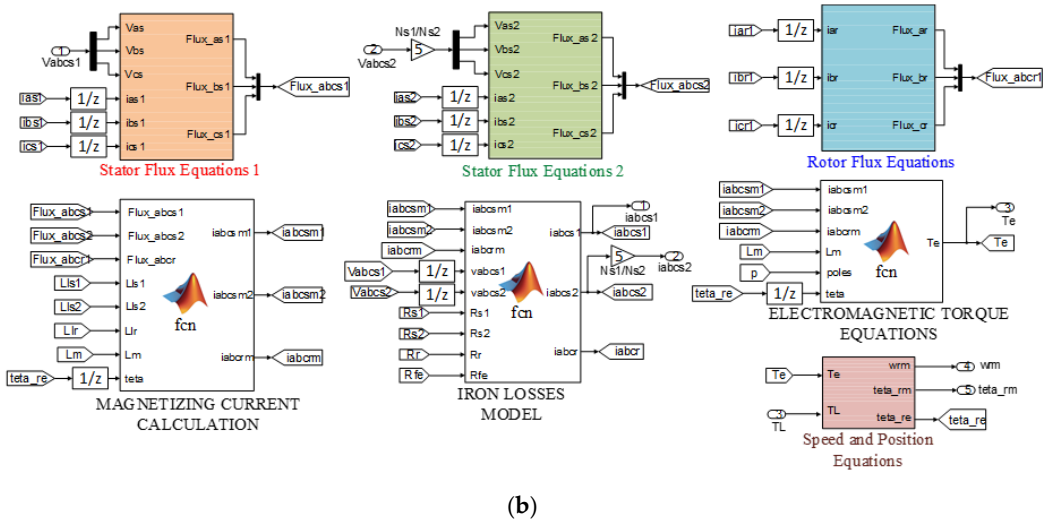
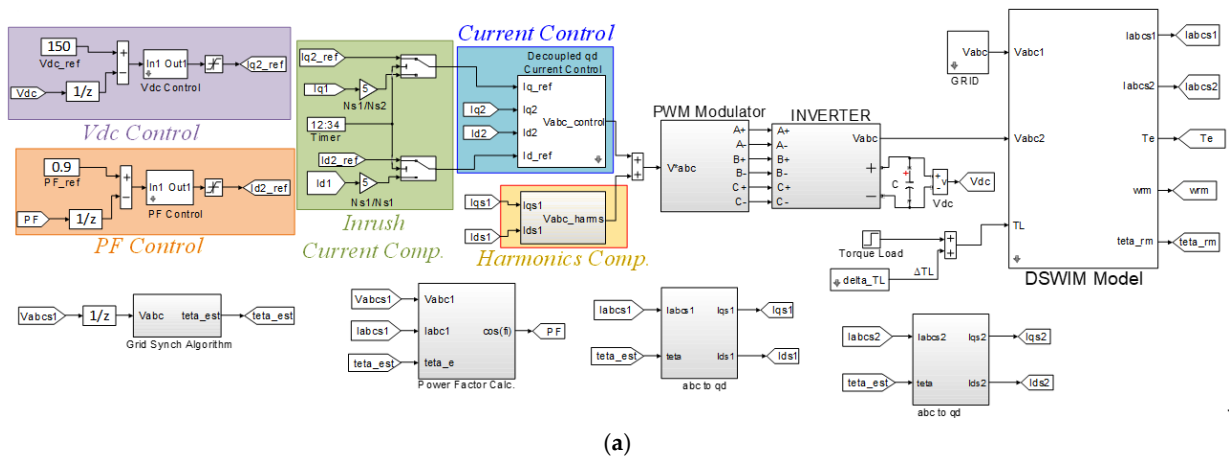


Figure 5. Simulink block diagram of the: (a) power conversion system and control strategies and (b) DOL-DWIM model.

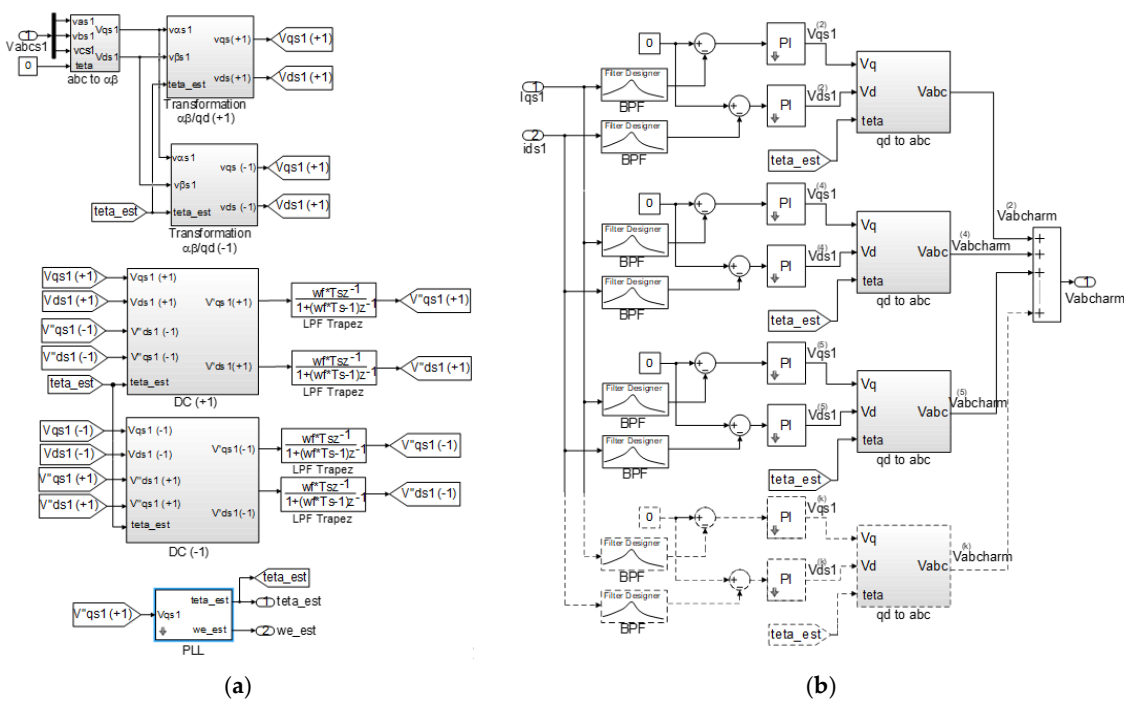


Figure 6. Simulink block diagram of the: (a) MSF algorithm and (b) harmonics compensation.

A first set of tests dealt with assessing the capability of the proposed solution to regulate the reactive power exchange between the power conversion system and the AC grid in a wide operating range. The performance of a standard IM featuring a single stator winding was compared with that of the DWIM under same load conditions. Active and reactive power flows associated to the fundamental harmonics in both main and auxiliary windings are shown in Figure 7. The simulation results are shown in Figure 8.

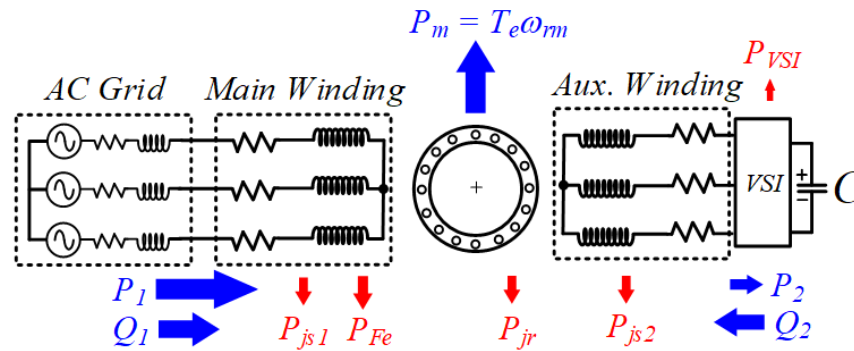


Figure 7. Power flow scheme of the DWIM.

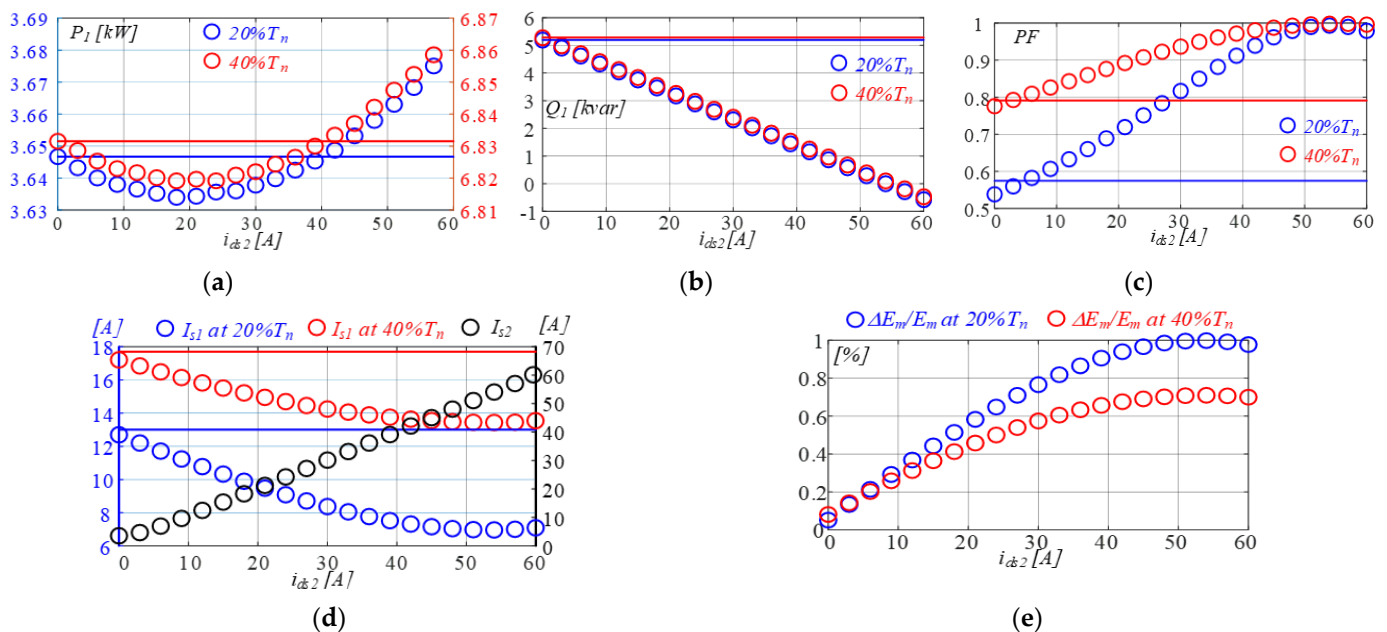


Figure 8. (a) Active and reactive power (P_1 and Q_1 , respectively), (b) power factor PF , (c) main winding current magnitude I_{s1} , (d) auxiliary winding current magnitude I_{s2} , (e) p.u. back-electromotive force (EMF) variation ΔE_m , computed at 20% and 40% of rated torque T_n for different values of i_{ds2} (solid lines—standard IM; circles—DWIM).

The active power P_1 and reactive power Q_1 absorbed by the DWIM are reported in Figure 8a,b as a function of the current i_{ds2} . The magnitude of currents in both windings, PF, and the per-unit (p.u.) variation of the back-electromotive force (EMF) E_m are displayed in Figure 8c–e, respectively, considering two different load conditions: 20% and 40% of the rated torque. The same figures include the corresponding quantities computed for the single-winding IM configuration (the same electrical machine without auxiliary winding) operating under the same load conditions, whose values are indicated in the figures with horizontal solid lines. By varying i_{ds2} , a beneficial effect is achieved, consisting of a reduction in Q_1 and leading to an improved PF (Figure 8c). This causes a reduction in the current flowing through the main winding, as shown in Figure 8d. This last result is justified even by the increase in the back-emf E_m of the DWIM in correspondence with

an increase in i_{ds2} , as clearly shown in Figure 8e; the last variation is in any case limited to a few percentages of the back-EMF of the DWIM with $i_{ds2} = 0$. The variation in E_m is associated to a variation in the magnetizing current.

The proposed approach can lead to a reduction in the active power P_1 absorbed by the DWIM at partial load, leading to an efficiency improvement. This result is confirmed by the analysis summarized in Figure 9, where the iron and total Joule losses are computed for the standard single-winding IM configuration and the considered DWIM as a function of the current i_{ds2} . In particular, Figure 9 displays the difference between the standard IM and DWIM total Joule losses ΔP_j (stator and rotor) and iron losses ΔP_{Fe} , with both motors operating under the same loads. The joule P_j and iron P_{Fe} losses referring to the single-winding IM are the points displayed in the three graphs at $i_{ds2} = 0$. Notably, in DWIM, by increasing i_{ds2} , iron losses rise and total joule losses initially drop and then rise. Thus, by suitably selecting i_{ds2} , the balance between iron losses increase and joule losses drop may lead to a neat reduction in total power losses and to a higher efficiency compared with the conventional IM. This beneficial result is strictly related to the motor design, load condition, and desired power factor PF. If we assume to operate the DWIM at PF = 0.9, thus requiring $i_{ds2} \approx 25A$ (Figure 8c) and a load equal to 40% T_n , a total loss reduction ΔP_{loss} equal to 3% can be achieved compared with the standard IM configuration. On the contrary, the same DWIM operated at PF = 0.9 and a load equal to 20% T_n , will require a $i_{ds2} = 40A$, yielding a $\Delta P_{loss}/P_{loss}$ less than 0.8%, significantly reducing the efficiency improvement of the DWIM. The implementation of a losses minimization algorithm is not the focus of the paper, and more details on how to approach this aspect can be found in [30].

Simulations were performed over a wide load range and the results shown in Figure 10 confirm the effectiveness of the proposed approach in increasing the power factor by acting on i_{ds2} with marginal variations in the additional power losses, although the improvement becomes progressively less relevant as the load increases.

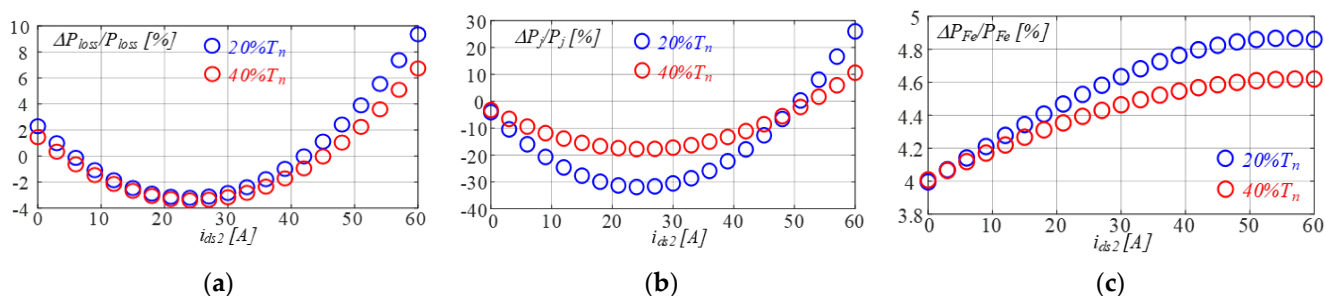


Figure 9. (a) Total loss variation in p.u. ΔP_{loss} , (b) joule losses variation in p.u. ΔP_j , and (c) iron losses variation in p.u. ΔP_{Fe} , vs. i_{ds2} , computed at 20% and 40% of rated torque T_n . Joule P_j and iron P_{Fe} losses referring to the single-winding IM are the points displayed in the three graphs at $i_{ds2} = 0$.

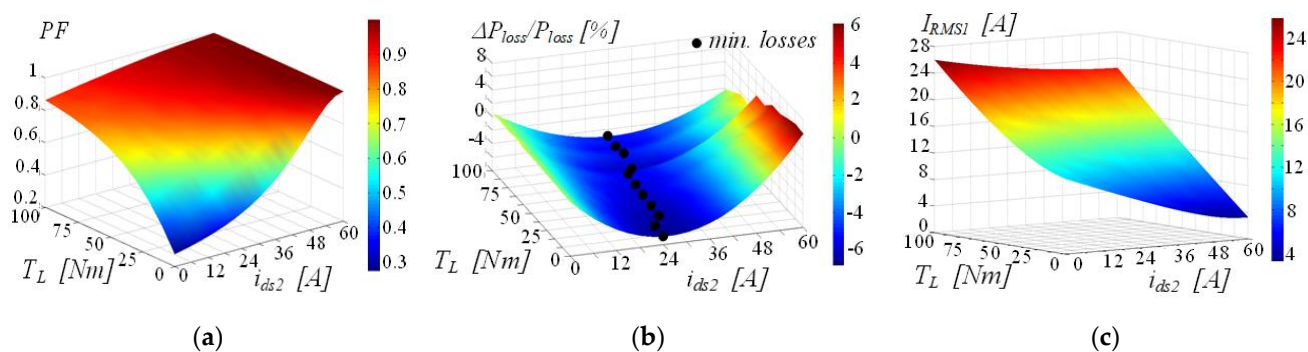


Figure 10. (a) PF, (b) ΔP_{loss} , (c) root mean square (RMS) value of the main winding current I_{RMS1} , determined under different loads T_L .

According to Figure 10b, for a given load condition, negative losses ΔP_{loss} can be achieved by suitably selecting i_{ds2} , leading to higher efficiency compared with the standard IM. Figure 11 deals with some results obtained by holding the PF at 0.9 by means of the control system. As shown, under constant PF operation, i_{ds2} and the reactive power Q_2 decrease when decreasing the load torque and the absorbed active power. Moreover, only a small active power P_2 is transferred from the grid to the auxiliary winding. Finally, both the active power P_1 and reactive power Q_1 are changed by the controller in order to keep the power factor constant. The power handled by the auxiliary winding in the worst-case scenario, i.e., a very light load, is roughly one-fifth of the standard IM rated power.

The dynamic behavior of the PF controller was also evaluated and some results are shown in Figure 12, dealing with a sequence of step loads T_L using a standard DOL IM and the proposed DOL DWIM. A rather satisfying dynamic behavior was achieved with the DOL DWIM, which was able to hold the PF constant.

The test results shown in Figure 13a confirm the effectiveness of the proposed approach in mitigating the oscillations of the rotational speed caused by an externally applied sinusoidal shaft torque disturbance $\Delta T_L = 20$ Nm (20% of rated torque) at 100 Hz. We note the remarkable speed ripple reduction after the instant t_1 , when the current control in the auxiliary winding set is activated.

Figure 13b depicts the mitigation of the speed ripple generated by a fifth harmonic component ($f_d = 250$ Hz) superimposed to the fundamental AC grid voltage. At t_1 , the compensation algorithm is turned on, leading to the reduction in the speed ripple. A very small V_{dc} ripple was also observed in both cases.

The effects of the harmonic compensation on motor quantities are shown in Figure 14. The obtained results confirmed the theoretical harmonic distribution given by Equation (15). Specifically, a second-order harmonic disturbance on the electromagnetic torque and on the mechanical speed produced a harmonic of the same order on the qd axis currents and therefore a third harmonic disturbance in the phase currents on both main and auxiliary windings. A different case is considered in Figure 15, where a fifth harmonic component is superimposed on the AC grid voltage. The theoretical findings and the effectiveness of the harmonic compensation were also confirmed in this case.

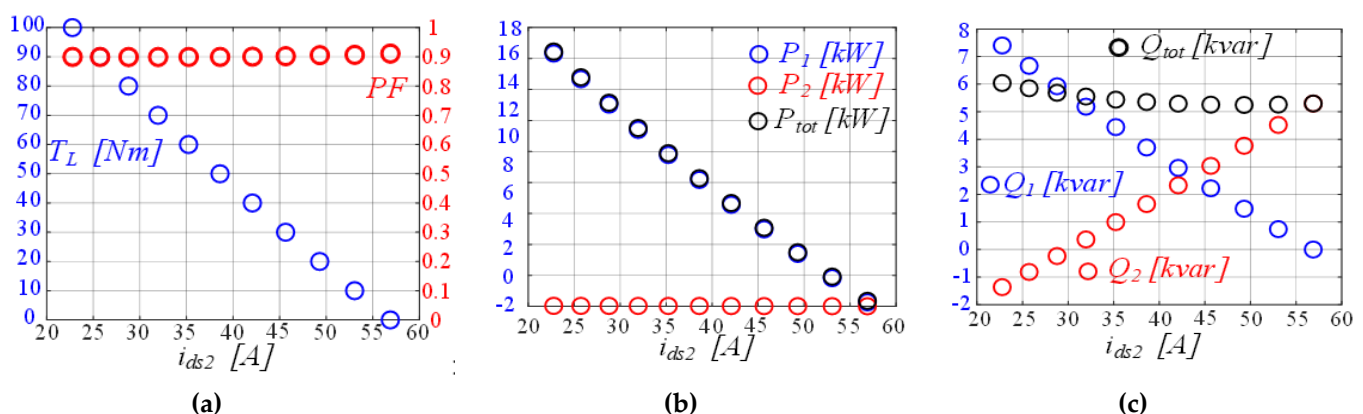


Figure 11. (a) Power factor control: T_L and PF vs. i_{ds2} ; (b) P_1 , P_2 , $P_{tot} = P_1 + P_2$; (c) Q_1 , Q_2 and $Q_{tot} = Q_1 + Q_2$.

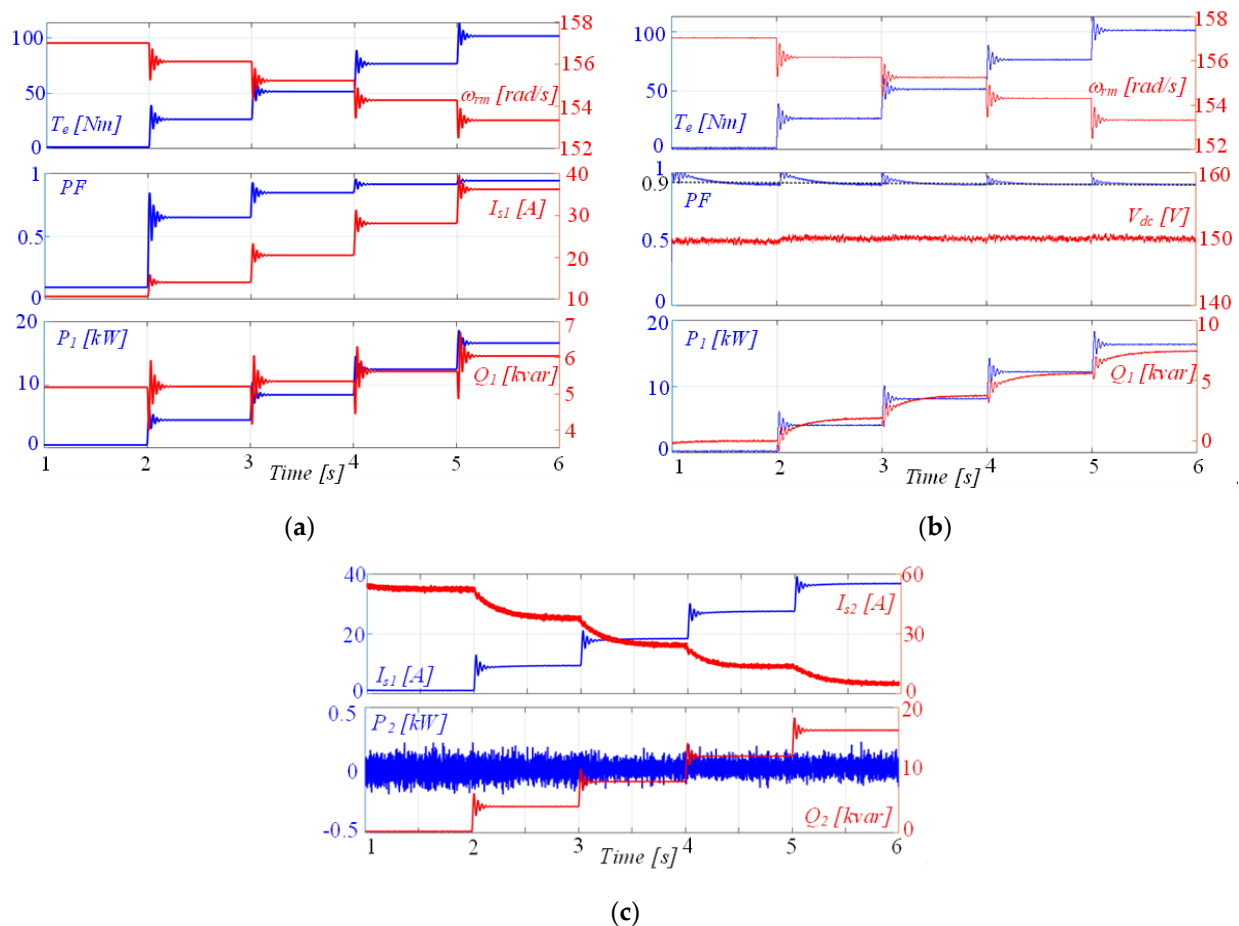


Figure 12. Dynamic transients under different torque load TL conditions: (a) in standard IM configuration and (b,c) in the proposed DWIM configuration.

Finally, the effectiveness of the proposed approach in mitigating inrush currents was evaluated by considering two motors rated at 3 and 15 kW. Figure 16 shows the currents in the two windings during the start-up without and with using the proposed technique for peak current reduction on the two motors. Figure 16a deals with the 3 kW IM using a 5 mF flying capacitor, whereas Figure 16b deals with the 15 kW machine using 120 mF capacitor. In both cases, at $t = t_2$, the current control is disabled and the PF and V_{dc} controls are activated instead. A remarkable mitigation of the grid current was obtained, as well as an increase of the electromagnetic torque, although at the cost of rather high transitory currents on the auxiliary winding. The floating capacitor has to be charged before the start-up of the DOL DWIM. This goal can be reached in different ways by using low-power, low-voltage circuitries. A viable solution is presented in Figure 17, where a cascade connection of a small power transformer and diode rectifier was used to charge the floating capacitor. The performance in terms of inrush line current mitigation clearly improved by increasing the capacitance of the floating capacitor because this reduced the power drawn from the grid. However, a large flying capacitor may be impractical in some applications; hence, a smaller capacitor complemented by a parallel connected battery can be used instead. An alternative approach consists of operating the start-up at a higher DC-bus voltage in order to increase the energy stored in the floating capacitor. A cost-benefit analysis is also required to establish the inverter ratings and thus the overcurrent mitigation level during the start-up.

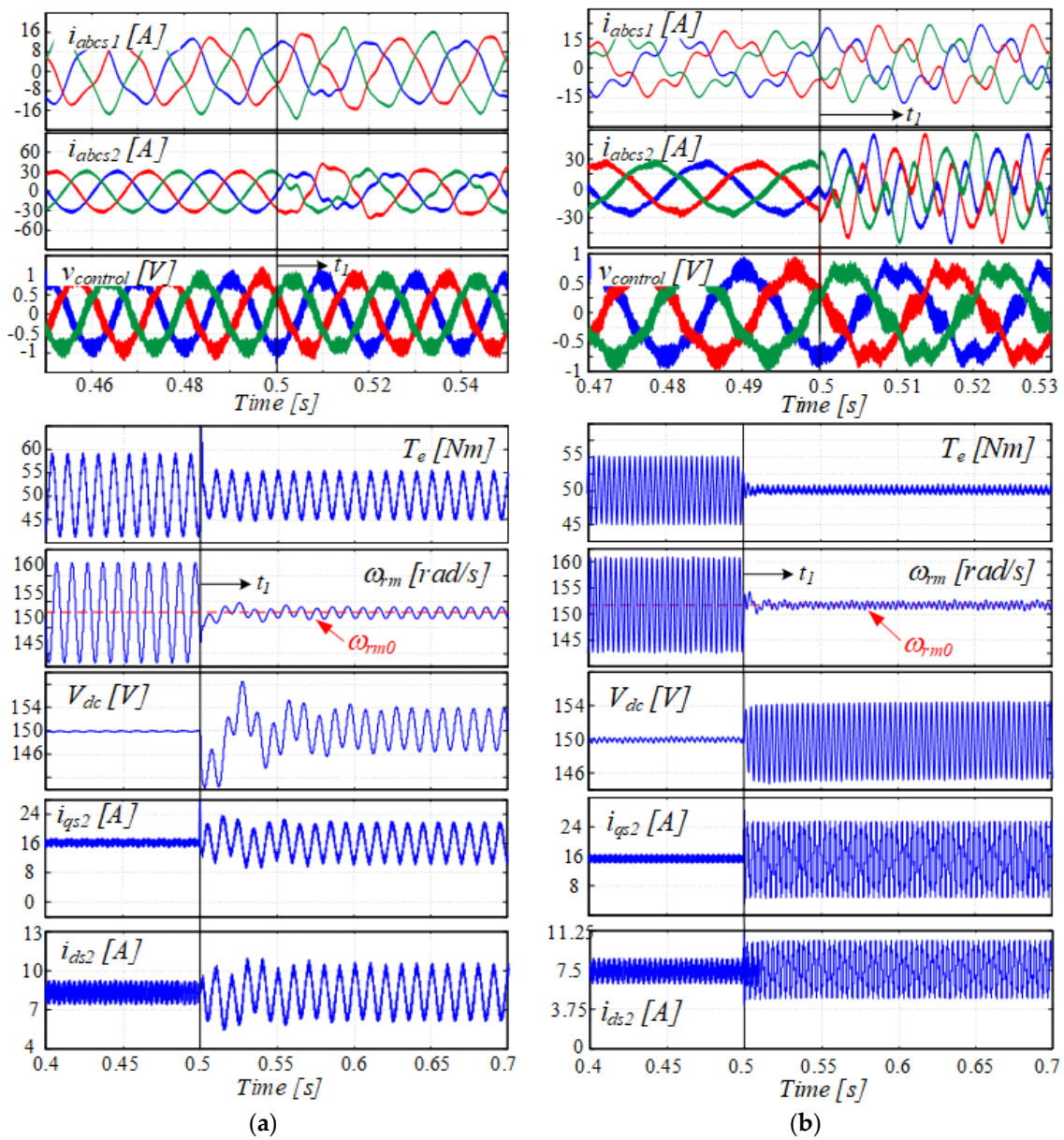


Figure 13. Simulation results: (a) compensation of ω_{rm} with $\Delta TL = 20 \text{ Nm}$; (b) compensation of ω_{rm} with $V_{abc5th} = 30 \text{ V}$.

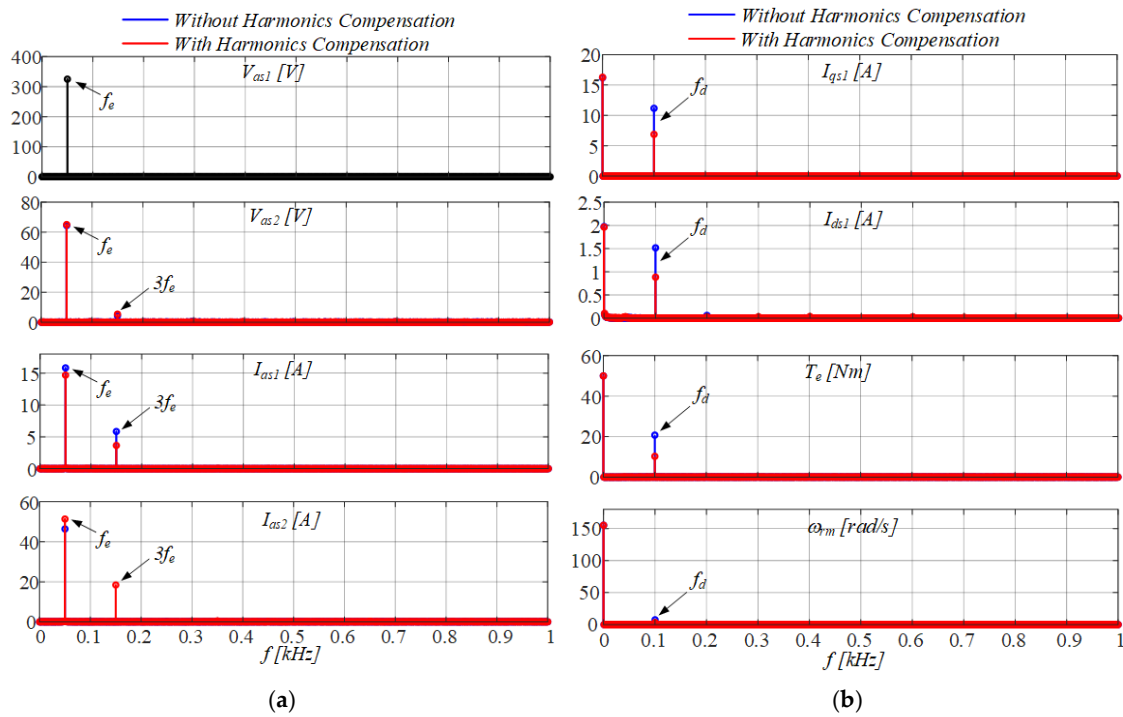


Figure 14. Harmonic content of motor quantities with and without the harmonic compensation when a sinusoidal torque disturbance is applied to the shaft: (a) main winding phase stator amplitude voltage V_{as1} , auxiliary winding phase stator voltage amplitude V_{as2} , main winding phase stator amplitude current I_{as1} , auxiliary winding phase stator amplitude current I_{as2} ; (b) qd-axes main winding stator current I_{qs1} and I_{ds1} , electromagnetic torque T_e , mechanical speed ω_{rm} .

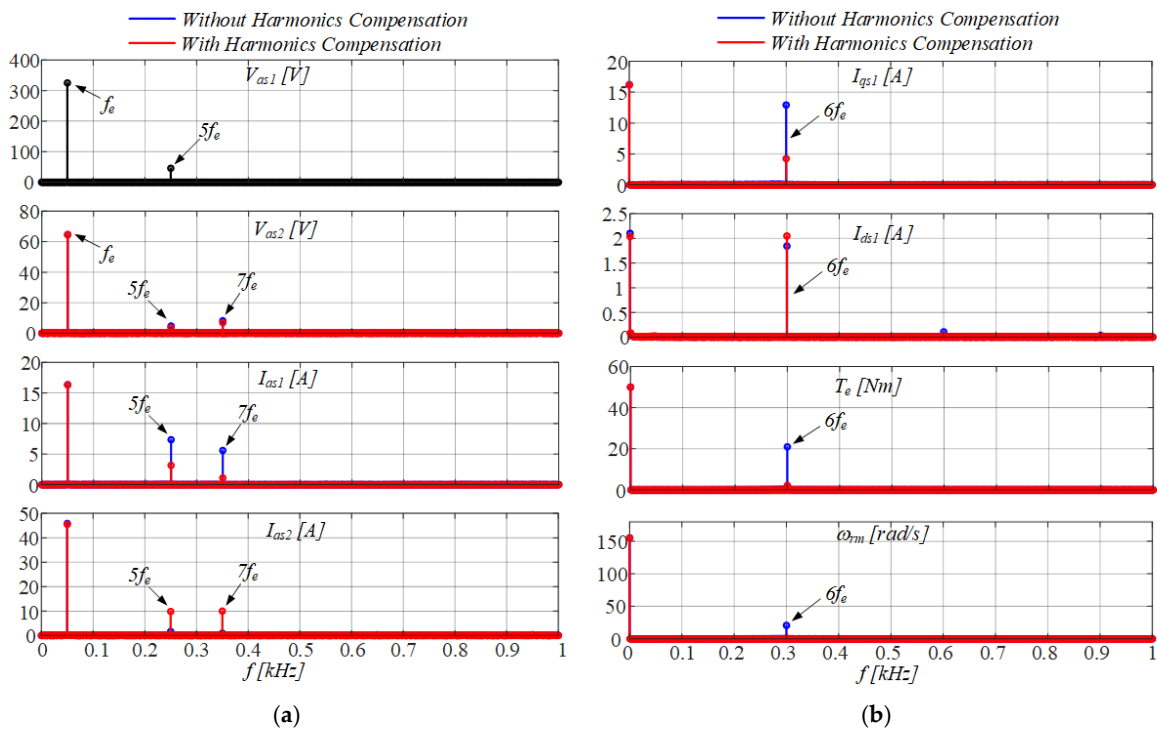


Figure 15. Harmonic content of motor quantities with and without harmonic compensation when a 5th harmonic component is superimposed on the AC grid voltage: (a) main winding phase stator amplitude voltage V_{as1} , auxiliary winding phase stator voltage amplitude V_{as2} , main winding phase stator amplitude current I_{as1} , auxiliary winding phase stator amplitude current I_{as2} ; (b) qd-axes main winding stator current I_{qs1} and I_{ds1} , electromagnetic torque T_e , mechanical speed ω_{rm} .

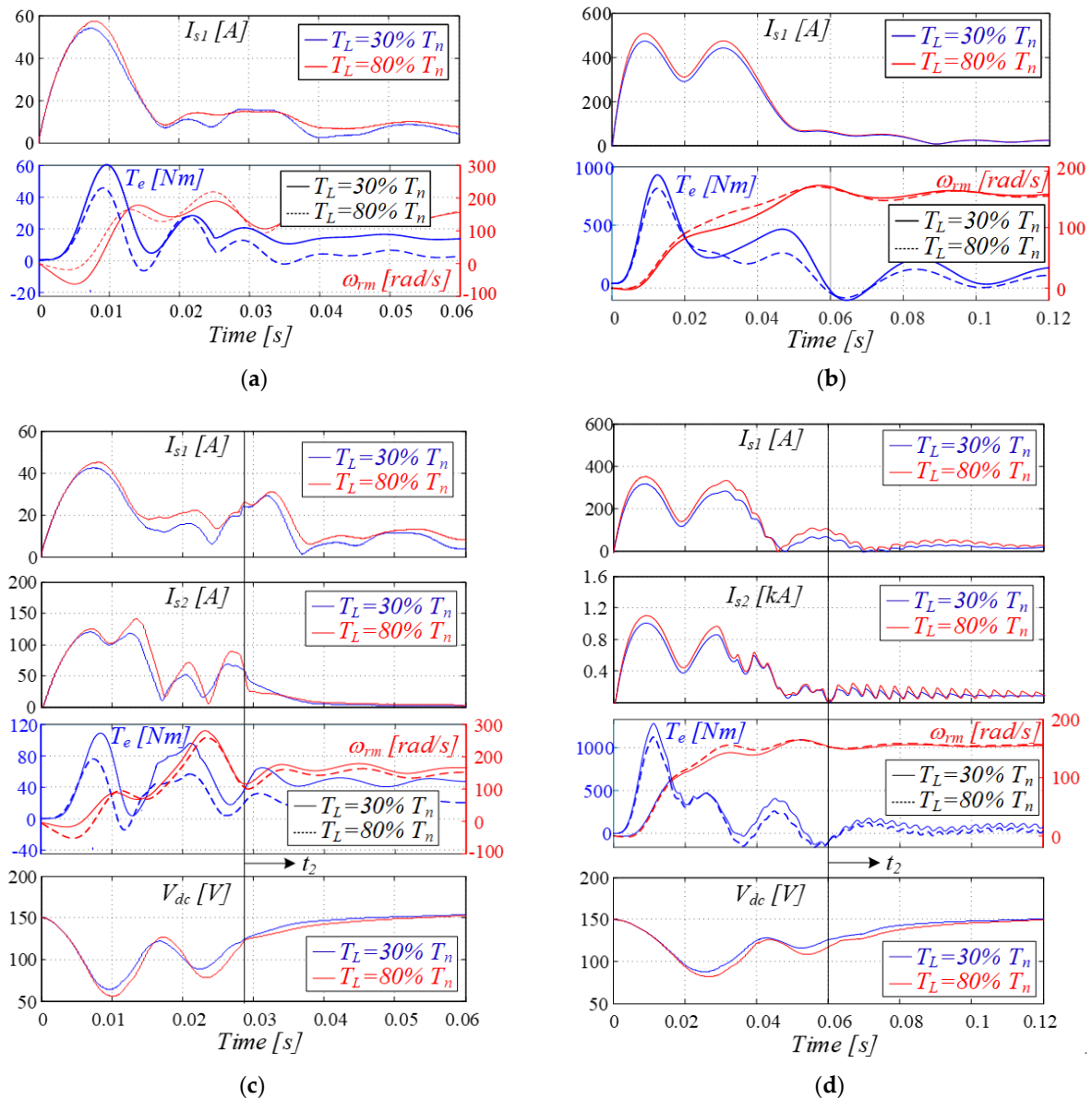


Figure 16. Induction motor start-up current: (a) standard IM (3 kW), (b) standard IM (15 kW), (c) 3 kW with the proposed technique, and (d) 15 kW with the proposed technique.

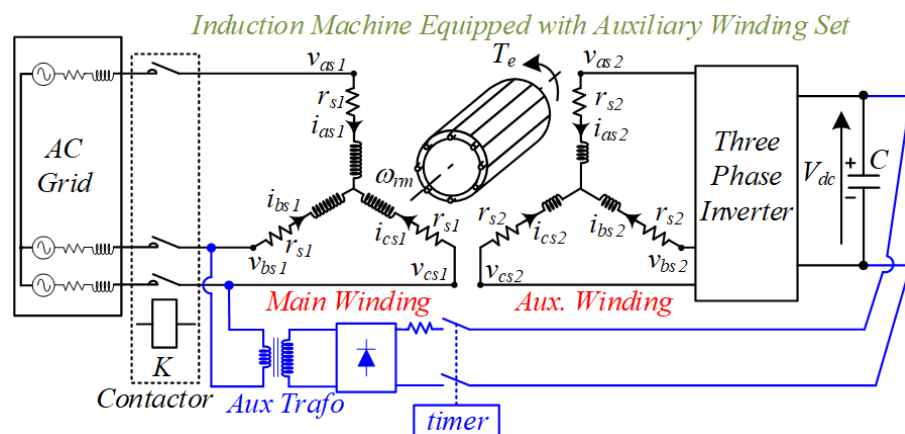


Figure 17. Floating capacitor low-power, low-voltage charging circuit.

5. Conclusions

The main aim of this paper was to demonstrate that the performance of direct line connected induction motors can be improved by introducing an auxiliary stator winding supplied by a partial power inverter. The auxiliary stator winding features fewer turns than the main one, and thus has lower voltage and power ratings. However, if suitably controlled, the additional winding allows for the achievement of an effective power factor control and a compensation of torque oscillations produced by the mechanical load or by distorted utility grid voltages. Moreover, under certain conditions, it is possible to mitigate the line overcurrent occurring during the start-up of the induction machine. The proposed solution is expected to be mainly applied for medium–high power range motors, where the cost of the system could be more affordable.

Author Contributions: G.S. (Giacomo Scelba) and L.D.T. conceived the original idea. M.C., S.F. and L.D.T. developed the theory and performed the computations. A.T., G.S. (Giuseppe Scarcella), S.A.R. and S.D.C. verified the analytical methods. All authors discussed the results and contributed to the final manuscript. All authors have read and agreed to the published version of the manuscript.

Funding: This work has been partially supported by the University of Catania under the interdepartmental project PIA.CE.RI. 2020–2022 Line 2-TMESPEMES.

Institutional Review Board Statement: Not applicable.

Informed Consent Statement: Informed consent was obtained from all subjects involved in the study.

Data Availability Statement: Not applicable.

Conflicts of Interest: The authors declare no conflict of interest.

References

1. G1 IEC 60034-30-1:2014. *Rotating Electrical Machines—Part 30-1: Efficiency Classes of Line Operated AC Motors*; IEC: Geneva, Switzerland, 2014.
2. Morimoto, S.; Tong, Y.; Takeda, Y.; Hirasu, T. Loss minimization control of permanent magnet synchronous motor drives. *IEEE Trans. Ind. Electron.* **1994**, *41*, 511–517. [[CrossRef](#)]
3. Kim, S.; Yoon, Y.; Sul, S.; Ide, K. Maximum Torque per Ampere (MTPA) Control of an IPM Machine Based on Signal Injection Considering Inductance Saturation. *IEEE Trans. Power Electron.* **2013**, *28*, 488–497. [[CrossRef](#)]
4. Uddin, M.N.; Nam, S.W. New Online Loss-Minimization-Based Control of an Induction Motor Drive. *IEEE Trans. Power Electron.* **2008**, *23*, 926–933. [[CrossRef](#)]
5. Cacciato, M.; Consoli, A.; Scarcella, G.; Scelba, G. Indirect maximum torque per ampere control of induction motor drives. In Proceedings of the EPE, Aalb, Den, 2–5 September 2007; pp. 1–10.
6. Attaianese, C.; Perfetto, A.; Tomasso, G. A space vector modulation algorithm for torque control of inverter fed induction motor drive. *IEEE Trans. Energy Convers.* **2002**, *17*, 222–228. [[CrossRef](#)]
7. Kim, H.-J.; Lee, H.-D.; Sul, S.-K. A new PWM strategy for common-mode voltage reduction in neutral-point-clamped inverter-fed AC motor drives. *IEEE Trans. Ind. Appl.* **2001**, *37*, 1840–1845.
8. Hava, A.M.; Kerkman, R.J.; Lipo, T.A. Carrier-based PWM-VSI overmodulation strategies: Analysis, comparison, and design. *IEEE Trans. Power Electron.* **1998**, *13*, 674–689. [[CrossRef](#)]
9. Zhong, E.; Lipo, T.A. Improvements in EMC performance of inverter-fed motor drives. *IEEE Trans. Ind. Appl.* **1995**, *31*, 1247–1256. [[CrossRef](#)]
10. Cacciato, M.; Caro, S.D.; Scarcella, G.; Scelba, G.; Testa, A. Improved space-vector modulation technique for common mode currents reduction. *IET Power Electron.* **2013**, *6*, 1248–1256. [[CrossRef](#)]
11. Cacciato, M.; Consoli, A.; Scarcella, G.; Scelba, G.; Testa, A. A novel space-vector modulation technique for common mode emissions reduction. In Proceedings of the International Aegean Conference on Electrical Machines and Power Electronics, Bodrum, Turkey, 2–4 September 2007; pp. 199–204.
12. Muljadi, E.; Lipo, T.A.; Novotny, D.W. Power Factor Enhancement of Induction Machines by Means of Solid-State Excitation. *IEEE Trans. Power Electron.* **1989**, *4*, 409–418. [[CrossRef](#)]
13. Spée, R.; Wallace, A.K. Comparative Evaluation of Power Factor Improvement Techniques for Squirrel Cage Induction Motors. *IEEE Trans. Ind. Appl.* **1992**, *28*, 381–386. [[CrossRef](#)]
14. Basak, S.; Chakraborty, C. Dual Stator Winding Induction Machine: Problems, Progress, and Future Scope. *IEEE Trans. Ind. Electron.* **2015**, *62*, 4641–4652. [[CrossRef](#)]

15. Muteba, M.C.; Jimoh, A.A.; Nicolae, D.V. Improving three-phase induction machines power factor using single phase auxiliary winding fed by an active power filter. In Proceedings of the IEEE Conference AFRICON, Windhoek, South Africa, 13–15 September 2007; pp. 1–7.
16. Malik, N.; Sadarangani, C.; Cosic, A.; Lindmark, M. Induction Machine at Uniy Power Factor with Rotating Power Electronic Converter. In Proceedings of the IEEE International Symposium SPEEDAM, Sorrento, Italy, 24–26 June 2012; pp. 401–408.
17. Knight, A.M.; Salomon, J.C.; Haque, R.; Perera, N.; Toulabi, M.S. A grid-connected induction machine capable of operation at unity and leading power factor. In Proceedings of the IEEE Energy Conversion Congress and Exposition, Denver, CO, USA, 10–14 October 2013; pp. 238–245.
18. Riley, C.M.; Lin, B.K.; Habetler, T.G.; Kliman, G.B. Stator current harmonics and their causal vibrations: A preliminary investigation of sensorless vibration monitoring applications. *IEEE Trans. Ind. Appl.* **1999**, *35*, 94–99. [[CrossRef](#)]
19. Foti, S.; De Caro, S.; Testa, A.; Tornello, L.D.; Scelba, G.; Scarcella, G. Grid-Connected Open-end Winding Induction Motor Drives. In Proceedings of the International Symposium SPEEDAM, Sorrento, Italy, 24–26 June 2020; pp. 30–35.
20. Basak, S.; Chakraborty, C.; Sinha, A.K. Dual Stator Induction Generator with Controllable Reactive Power Capability. In Proceedings of the IEEE Symposium ISIE, Instabul, Turkey, 1–4 June 2014; pp. 2584–2589.
21. Marouani, K.; Nounou, K.; Benbouzid, M.; Tabbache, B. Power factor correction of an electrical drive system based on multiphase machines. In Proceedings of the IEEE First International Conference on Green Energy ICGE, Sfax, Tunisia, 25–27 March 2014; pp. 152–157.
22. Ojo, O.; Davidson, I.E. PWM-VSI inverter-assisted stand-alone dual stator winding induction generator. *IEEE Trans. Ind. Appl.* **2000**, *36*, 1604–1611.
23. Li, Y.; Hu, Y.; Huang, W.; Liu, L.; Zhang, Y. The Capacity Optimization for the Static Excitation Controller of the Dual-Stator-Winding Induction Generator Operating in a Wide Speed Range. *IEEE Trans. Ind. Electron.* **2009**, *56*, 530–541.
24. Levi, E.; Sokola, M.; Boglietti, A.; Pastorelli, M. Iron loss in rotor-flux-oriented induction machines: Identification, assessment of detuning, and compensation. *IEEE Trans. Power Electron.* **1996**, *11*, 698–709. [[CrossRef](#)]
25. Scarcella, G.; Scelba, G.; Cacciato, M.; Spampinato, A.; Harbaugh, M.M. Vector Control Strategy for Multidirectional Power Flow in Integrated Multidrive Starter-Alternator Applications. *IEEE Trans. Ind. Appl.* **2016**, *52*, 4816–4826. [[CrossRef](#)]
26. Wee, S.-D.; Shin, M.-H.; Hyun, D.-S. Stator-flux-oriented control of induction motor considering iron loss. *IEEE Trans. Ind. Electron.* **2001**, *48*, 602–608.
27. Golestan, S.; Guerrero, J.M.; Vasquez, J.C. Single-Phase PLLs: A Review of Recent Advances. *IEEE Trans. Power Electron.* **2017**, *32*, 9013–9030. [[CrossRef](#)]
28. Zou, Z.; Liserre, M. Modeling Phase-Locked Loop-Based Synchronization in Grid-Interfaced Converters. *IEEE Trans. Energy Convers.* **2020**, *35*, 394–404. [[CrossRef](#)]
29. De Donato, G.; De Scelba, G.; Borocci, G.; Capponi, F.G.; Scarcella, G. Fault-Decoupled Instantaneous Frequency and Phase Angle Estimation for Three-Phase Grid-Connected Inverters. *IEEE Trans. Power Electron.* **2016**, *31*, 2880–2889. [[CrossRef](#)]
30. Nobile, G.; Scelba, G.; Cacciato, M.; Scarcella, G. Losses Minimization Control for an Integrated Multidrive Topology Devoted to Hybrid Electric Vehicles. *IEEE Trans. Ind. Electron.* **2019**, *66*, 8345–8360. [[CrossRef](#)]